The Universe is Brighter in the Direction of Our Motion: Galaxy Counts and Fluxes are Consistent with the CMB Dipole

Jeremy Darling [ORCID]
Center for Astrophysics and Space Astronomy, Department of Astrophysical and Planetary Sciences, University of Colorado, 389 UCB, Boulder, CO 80309-0389, USA; jeremy.darling@colorado.edu

Abstract

An observer moving with respect to the cosmic rest frame should observe a concentration and brightening of galaxies in the direction of motion and a spreading and dimming in the opposite direction. The velocity inferred from this dipole should match that of the cosmic microwave background (CMB) temperature dipole if galaxies are on average at rest with respect to the CMB rest frame. However, recent studies have claimed a many-fold enhancement of galaxy counts and flux in the direction of the solar motion compared to the CMB expectation, calling into question the standard cosmology. Here we show that the sky distribution and brightness of extragalactic radio sources are consistent with the CMB dipole in direction and velocity. We use the first epoch of the Very Large Array Sky Survey combined with the Rapid Australian Square Kilometer Array Pathfinder Continuum Survey to estimate the dipole via several different methods, and all show similar results. Typical fits find a 331^{+161}_{-107} km s^{-1} velocity dipole with apex $(\ell, b) = (271^{+55}_{-58}, 56^{+13}_{-35})$ in Galactic coordinates from source counts and 399^{+264}_{-199} km s^{-1} toward $(\ell, b) = (301^{+30}_{-30}, 43^{+19}_{-17})$ from radio fluxes. These are consistent with the CMB-solar velocity, 370 km s^{-1} toward $(\ell, b) = (264, 48)$, and show that galaxies are on average at rest with respect to the rest frame of the early universe, as predicted by the canonical cosmology.

1. Introduction

The cosmic microwave background (CMB) shows a 3.4 mK dipole that is interpreted as a peculiar solar motion with respect to the CMB rest frame (Smoot et al. 1977). If this interpretation is correct, then our canonical cosmology predicts that galaxies should show a corresponding dipole in apparent number density and brightness (Ellis & Baldwin 1984). Galaxies should also show a secular parallax dipole in their proper motions (Ding & Croft 2009; Paine et al. 2020; Croft 2021). Detection of a galaxy number, flux, or parallax dipole that is in agreement with the CMB dipole would confirm the usual interpretation of the CMB dipole and indicate that the galaxy sample is on average at rest with respect to the CMB rest frame.

Previous work using radio galaxy counts and/or flux has produced mixed and contradictory results, often using the same data sources, including the 1.4 GHz NRAO VLA Sky Survey (NVSS; Condon et al. 1998), the 843 MHz Sydney University Molonglo Sky Survey (SUMSS; Murphy et al. 2007), the 325 MHz Westerbork Northern Sky Survey (WENSS; Rengelink et al. 1997), and the 147 MHz TIFR GMRT Sky Survey (TGSS-ADR1; Intema et al. 2017). Blake & Wall (2002) found NVSS counts that were consistent with the CMB dipole. Subsequent studies, including those based on the NVSS, found rough agreement with the CMB dipole direction but higher than expected dipole amplitude, of order 1%–6% variation rather than the canonical ∼0.5% amplitude, and

therefore excluded the CMB-solar velocity with high confidence (e.g., Singal 2011; Rubart & Schwarz 2013; Tiwari & Aluri 2019; Siewert et al. 2021). Gibelyou & Huterer (2012) found significant disagreement with the CMB in direction and amplitude. In infrared bands, Secrest et al. (2021) used a quasar catalog selected from the Wide-field Infrared Survey Explorer (WISE; Wright et al. 2010) to reject the kinematic interpretation of the CMB dipole at 4.9σ significance. Other infrared work focused on low-redshift galaxies that may be significantly influenced by large-scale structures (e.g., Gibelyou & Huterer 2012).

Consistency of extragalactic objects with the CMB dipole has been found in galaxy redshift surveys (e.g., Rowan-Robinson et al. 1990; Lavaux et al. 2010), in the modulation of the thermal Sunyaev–Zeldovich effect (tSZ; Planck Collaboration et al. 2020c), and in supernovae (Horstmann et al. 2021), suggesting that the discrepancy lies with galaxy and quasar surveys rather than with the canonical cosmology, large-scale structures, or lensing, as some authors have suggested.

In this work, we employ two new radio continuum surveys, the Karl G. Jansky Very Large Array[1] Sky Survey (VLASS; Lacy et al. 2020) in the northern hemisphere and the Rapid Australian Square Kilometer Array Pathfinder[2] Continuum Survey (RACS; McConnell et al. 2020) in the south to measure the galaxy number and flux dipoles using nearly complete (90%) sky coverage. We present the theoretical expectations for galaxy dipoles in number and flux in Section 2; we discuss

---

[1] The National Radio Astronomy Observatory is a facility of the National Science Foundation operated under a cooperative agreement by Associated Universities, Inc.

[2] The Australian SKA Pathfinder is part of the Australia Telescope National Facility which is managed by CSIRO.

the data sources, catalog-matching, and map-making in Section 3; and we describe four different dipole measurement techniques for number and flux in Section 4. The results of these measurements are all self-consistent and in good agreement with the CMB dipole (Section 5), and it is not clear why this work produced such different results from previous studies (Section 6). We conclude with some suggestions for future improvement on this analysis, both in terms of technique and looking to future data from ongoing and planned continuum surveys (Section 7).

For comparison to the results in this work, we use the fiducial Planck Collaboration et al. (2020a, 2020b) CMB dipole: $3362.08 \pm 0.99\ \mu K$ toward galactic coordinates $(\ell, b) = (264°021 \pm 0°011, 48°253 \pm 0°005)$ or equatorial coordinates $(\alpha, \delta) = (167°942 \pm 0°007, -6°944 \pm 0°007)$ (J2000). Absent an intrinsic CMB dipole, the velocity of the Sun relative to the CMB is $369.82 \pm 0.11\ \mathrm{km\ s^{-1}}$.

2. Theoretical Expectations

Ellis & Baldwin (1984) showed how the number density of galaxies would be altered for an observer moving with respect to the CMB rest frame (see also Gibelyou & Huterer 2012; Rubart & Schwarz 2013). Briefly, starting with Lorentz-invariant quantities such as number N and a frequency-normalized specific intensity, I_ν/ν^3, which is the photon phase-space distribution, one can show that an observer Lorentz-boosted with respect to the average rest frame of galaxies will observe a dipole on the sky that depends on powers of the factor δ,

$$\delta = \gamma(1 + \hat{n} \cdot \boldsymbol{v}) = \frac{1 + v\cos\theta}{(1 - v^2)^{1/2}}, \tag{1}$$

for an observation in the direction $\hat{n}$ and boost $\boldsymbol{v}$ ($c \equiv 1$). The observed effects are (1) a relativistic Doppler shift, δ^1; (2) aberration, which alters solid angles as δ^2; (3) flux modification of objects with power-law spectral energy distributions $S_\nu \propto \nu^{-\alpha}$ when observed at fixed frequencies, $\delta^{1+\alpha}$; and (4) a change in the number of galaxies detected using a fixed flux limit, if $N(>S) \propto S^{-x}$, $\delta^{x(1+\alpha)}$. Combining these effects to first order in v, we expect the sky surface density of galaxies will be modulated by the angular distance θ from the dipole apex,

$$\frac{dN}{d\Omega} = \frac{dN}{d\Omega}\bigg|_{\theta = \pi/2} (1 + [2 + x(1 + \alpha)]\, v\cos\theta). \tag{2}$$

The expected fractional change in a monopole-subtracted sky would therefore be

$$\frac{\Delta N}{N_{\ell=0}} = [2 + x(1 + \alpha)]\, v\cos\theta. \tag{3}$$

The integrated flux density per solid angle brings an extra factor of $\delta^{1+\alpha}$, and the fractional change becomes

$$\frac{\Delta S}{S_{\ell=0}} = [3 + \alpha + x(1 + \alpha)]\, v\cos\theta. \tag{4}$$

This is the same quantity as the flux-weighted galaxy count (Rubart & Schwarz 2013). Turning Equations (3) and (4) around, for an observed null-centered (monopole-subtracted) dipole amplitude on the sky, $\mathcal{D}_N$ or $\mathcal{D}_S$, the observer's velocity

with respect to a galaxy catalog can be calculated:

$$v = \mathcal{D}_N/[2 + x(1 + \alpha)] \quad \text{or} \tag{5}$$

$$v = \mathcal{D}_S/[3 + \alpha + x(1 + \alpha)]. \tag{6}$$

If the galaxy catalog is at rest with respect to the CMB, then the measured velocity should match the CMB velocity dipole in direction and amplitude. The direction of the dipole is obtained from the apex coordinates.

In principle, the flux dipole should be more sensitive than the number because a higher signal-to-noise ratio can be obtained from flux measurements. But in practice, uniform flux calibration across a large survey (or multiple surveys) is challenging, and constraining systematics well below 1% is difficult. Simply counting well-detected sources is less challenging if one works above the survey completeness limit (although multicomponent radio sources can complicate the counting exercise).

3. Data

Sky dipole measurements require all-sky coverage, which can be done using space-based facilities such as WISE (Wright et al. 2010; Secrest et al. 2021), but require dual-hemisphere terrestrial surveys. For this work, we use two new radio continuum surveys: the VLASS at 3 GHz in the north (Lacy et al. 2020) and the RACS at 887.5 MHz in the south (McConnell et al. 2020).

The VLASS is a three-epoch synoptic survey spanning 2–4 GHz at declinations $\delta > -40°$ with $2''5$ angular resolution. The first epoch data release catalog includes 1.9×10^6 sources with 99.8% completeness at 3 mJy (Gordon et al. 2021). We select Duplicate_flag < 2, Quality_flag == 0, and $|b| > 5°$ from the Component Table (version 2) to obtain ~ 1.4 million sources. The first VLASS epoch was split (epochs 1.1 and 1.2) and the two subepochs show different noise properties and systematic flux density offsets compared to expectations (Gordon et al. 2021). Nevertheless, the $4° \times 10°$ survey tiling was interleaved somewhat[3] on angular scales much smaller than the $\ell = 1$ dipole scale, and our analysis does not include sources close to the detection limit or the portion of the survey that uses the hybrid array (see below). Following the advice of Gordon et al. (2021), all flux densities are scaled by $1/0.87$.

The RACS first data release catalog consists of ~ 2.1 million radio sources in declinations $-80° < \delta < +30°$ and $|b| > 5°$ with 95% point-source completeness at ~ 3 mJy (Hale et al. 2021), more than a factor of 3 below our adopted lower flux cutoff. This "RACS-low" release has a 288 MHz bandwidth centered at 887.5 MHz. The survey shows a spatially varying median rms noise structure between 0.1 and 0.6 mJy beam^{-1} on $\sim 5°$ scales and shows generally increasing noise with declination. The RACS survey was smoothed to a uniform $25''$ resolution.

All subsequent analysis uses the peak flux densities from these survey catalogs rather than integrated flux densities.[4] Peak flux densities are equivalent to integrated flux densities for unresolved radio sources and mitigate somewhat the

---

[3] Kimball, A. 2017, VLASS Project Memo #7: VLASS Tiling and Sky Coverage, https://library.nrao.edu/public/memos/vla/vlass/VLASS_007.pdf.

[4] We use the shorthand "flux" in subsequent discussion to generically refer to summed flux densities in map pixels and the peak flux densities of individual galaxies.
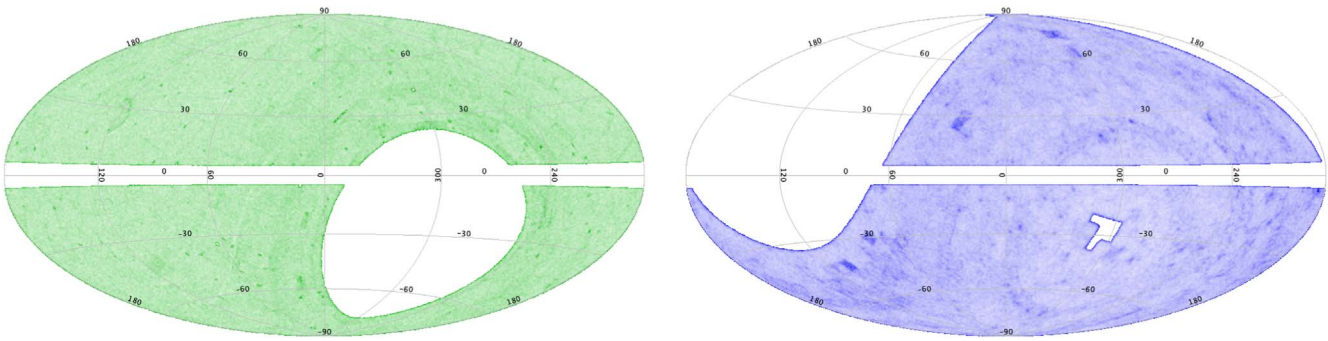
Figure 1. VLASS (left) and RACS (right) catalog sources in galactic coordinates. Darker color indicates fewer sources. $|b| < 5°$ was excluded from the VLASS.

angular scale and frequency mismatch between the VLASS and the RACS (see Figure 9 in Gordon et al. 2021 for an example of the relationship between peak and total flux density). The size of radio sources is a function of observed frequency and observing configuration, which complicates an all-sky analysis of source counts and flux using disparate surveys.

Figure 1 shows the two survey catalogs in Galactic coordinates before they are flux-selected, trimmed, masked, or combined. Figure 2 shows the number of sources in each catalog versus peak flux density prior to masking and trimming the samples. We select the VLASS 3–300 mJy beam^{-1} flux range[5] based on the linear part of the $\log N$–$\log S$ plot, staying well above the flux limit turnover at 1.3 mJy, which also reduces completeness issues caused by areally and temporally variable noise limits below the 3 mJy completeness limit, and well below the distribution turnover around 500 mJy. This selection also avoids stochastic contributions from bright radio sources. Using the spectral indices described in Section 3.1 below, we transfer the VLASS flux limits to the RACS catalog. The RACS limits for number counts and flux differ slightly but are well above the RACS 3 mJy survey completeness limit.

For the purposes of this analysis, absolute flux calibration is unimportant. Relative flux calibration across the sky does impact this study, but only if there are flux calibration systematics on steradian scales. The two-subepoch tiling pattern of the VLASS does not align with the CMB dipole and could not produce a spurious coincidentally aligned signal.

3.1. Catalog Matching

The VLASS shows elevated noise at $\delta > 80°$ and the RACS is incomplete at $\delta < -80°$, so we mask both surveys to exclude sources within 10° of the equatorial poles. We cut and combine the two surveys at $\delta = 0°$, which excludes each survey's lowest-elevation declination. range that tends to show higher noise and instrumental artifacts (Figure 1). We also mask the Galactic plane for $|b| < 5°$. Excluding a larger latitude range had little impact on results, and minimal masking reduces systematics and enhances the sky coverage (e.g., Siewert et al. 2021). We did no additional masking. The final maps cover a high sky fraction, $f_{sky} = 0.90$, and dipole measurements are therefore not expected to be significantly affected in amplitude or uncertainty by coupling to higher-order modes such as quadrupole or octopole (Gibelyou & Huterer 2012).
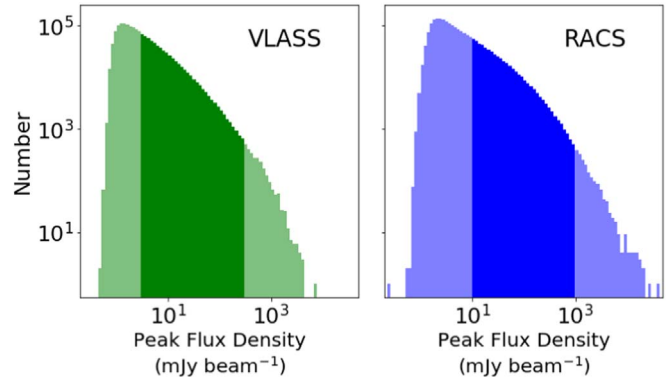
Figure 2. VLASS (left) and RACS (right) catalog source count vs. peak flux density. The opaque color indicates the catalog selection regions prior to masking and trimming.

For arbitrary flux limits, the two catalogs have differing source density and integrated flux density. This produces a dipole aligned with the equatorial poles. Because the expected signal is of order 0.5%, the catalog matching is crucial to the measurement and is extremely sensitive to the spectral index used to scale the RACS catalog at 887.5 MHz to the VLASS 3 GHz fluxes.

For any given 3 GHz flux density, the 3.0–0.9 GHz spectral index spans $\alpha = 1 \pm 2$, so any flux scaling to equalize the two surveys is only correct in aggregate and the total scaled flux is sensitive to the choice of the spectral index. Incorrect scaling leads to a hemispherical dipole (which is, in part, the reason we chose an equal-area division between the two surveys). We determine the median spectral index using the overlap region between the two surveys that is least affected by noise systematics, $-10° < \delta < +10°$ and $|b| > 5°$. The median spectral index is $\alpha = 0.98$, which we use to scale the flux limits of RACS to match those of the VLASS for the source number density analysis. For the flux analysis, we use the median RACS flux-weighted spectral index of $\alpha = 1.02$. These spectral indices are steeper than, but within the variance of, the 3–1.4 and 1.4–0.9 GHz spectral indices (Hale et al. 2021; Gordon et al. 2021).

The combined number catalog contains 711,450 sources, with a division of 49.9%–50.1%, VLASS to RACS. The combined flux catalog contains 697,753 sources, divided 50.9–49.1. The solid angle ratio of the unmasked portions of VLASS to RACS is 1.0006. The higher resolution of VLASS compared to RACS suggests that the VLASS would detect more objects per solid angle, but perhaps surprisingly, the areal density of sources in the surveys, after scaling flux limits, is the

---

[5] An upper flux cutoff does not alter the galaxy count or combined flux dependence on the δ factor.

same to within 0.2%, and a mismatch does not seem to obtain for the range shown in Figure 2.

The source count $N(>S) \propto S^{-x}$ index x can be determined empirically from the catalog: we find $x = 1.0$ for VLASS and RACS in the lower decade of the selected flux range, which dominates the source counts. The expected dipole amplitudes, based on the above α values and Equations (3) and (4), are therefore $\mathcal{D}_N = 4.0\ v = 0.0050$ for number and $\mathcal{D}_S = 6.1\ v = 0.0075$ for flux, assuming a null intrinsic CMB dipole (i.e., the dipole amplitude is solely caused by the barycenter motion with respect to the CMB rest frame). The observed dipole signals will therefore amount to less than 1% of the mean (monopole) count or flux value.

3.2. Map Making

To make number and flux maps, we create HEALPix[6] maps using `healpy`[7] with much finer resolution than the expected signal in order to create minimal-area masks. Mask-edge pixels, which incompletely sample the sky, are trimmed. Using `nside = 64` gives 49,152 pixels with a solid angle of 0.84 deg^2 per pixel. The median unmasked pixel contains 16 radio sources and 202 mJy (scaled to 3 GHz on the flux-corrected VLASS scale). Figure 3 (top) shows the mean-subtracted masked HEALPix number and flux maps.

Maps smoothed to 1 sr show structure at the 1%–3% level (Figure 3, middle), including a maximum in the vicinity of the CMB apex. However, all measurements described below use the unsmoothed masked maps or the combined catalog.

4. Measurements

We estimate the number and flux density dipoles using four methods: (1) by computing spherical harmonics (SH) components directly from the merged catalog (after Blake & Wall 2002); (2) by fitting SH to masked sky maps using the `healpy.anafast` algorithm; (3) using the dipole vector estimator employed by Secrest et al. (2021) on maps, `healpy.fit_dipole`; and (4) using a "permissive" fit of an SH dipole model to the maps that allows for outliers (Sivia & Skilling 2006; Darling et al. 2018).

(1) The direct method does not rely on making maps. Rather, it employs the standard method to calculate SH coefficients $a_{\ell,m}$ from N objects at (θ_i, ϕ_i):

$$a_{\ell,m} = \sum_{i=1}^{N} f_i\ Y^*_{\ell,m}(\theta_i, \phi_i), \qquad (7)$$

where $f_i = 1$ for number counts and $f_i = S_i$ for flux. For real f_i, the dipole map of a quantity becomes

$$f(\theta, \phi) = a_{1,0}Y_{1,0}(\theta, \phi) + 2\,a_{1,1}^{\mathfrak{R}}Y_{1,1}^{\mathfrak{R}}(\theta, \phi) - 2\,a_{1,1}^{\mathfrak{I}}Y_{1,1}^{\mathfrak{I}}(\theta, \phi). \qquad (8)$$

The amplitude of the dipole can be obtained by scaling the number N or flux S map maximum by the monopole

$$\mathcal{D}_{N,S} = \frac{f_{N,S}^{\max}}{a_{0,0}}\sqrt{\frac{4\pi}{3}}. \qquad (9)$$

Uncertainties in the dipole amplitude and direction are estimated by recalculating the dipole from a 10,000 iteration bootstrap resampling of the source catalog.

(2) The `anafast` SH method fits monopole and dipole SH coefficients to masked maps rather than data points. Masked regions are omitted from the fits, and data have been aggregated into equal-area pixels (either source counts or summed fluxes). Uncertainties are estimated from a nonparametric bootstrap (bootstrap resampling of fit residuals rather than data points). The parametric bootstrap uncertainties agree with the nonparametric implementation for the number maps but cannot be done on the flux maps.

(3) The dipole vector estimator described by Secrest et al. (2021) uses `healpy.fit_dipole` to simultaneously fit a monopole μ and a Cartesian 3D dipole vector $\boldsymbol{d}$ to maps. The fractional amplitude of the dipole signal is

$$\mathcal{D}_{N,S} = \frac{|\boldsymbol{d}_{N,S}|}{\mu}, \qquad (10)$$

and $\boldsymbol{d}$ points in the direction of the apex. We used a nonparametric bootstrap to estimate uncertainties.

(4) This method employs a "permissive" fit of an SH dipole to maps that does not assume Gaussian error distributions and thus allows for data outliers (such as clustered radio sources). We maximize the likelihood associated with a probability density function based on the data-model residual R_i of each pixel:

$$\mathrm{prob}(R_i) \propto \left(\frac{1 - e^{-R_i^2/2}}{R_i^2}\right) \qquad (11)$$

(Sivia & Skilling 2006; Darling et al. 2018). We use the Python package `lmfit`[8] to obtain least-squares fits of SH dipole coefficients and their marginalized uncertainties. We then use a Monte Carlo realization of those error budgets to determine the dipole velocity parameters and uncertainties (amplitude and direction).

5. Results

To calculate velocities from dipole amplitudes using Equations (5) and (6), we use the spectral index $\alpha = 0.98$ for number, $\alpha = 1.02$ for flux, and source-count index $x = 1.0$ for both (Section 3.1). Uncertainties are calculated using percentiles and are not always symmetric. We bias-correct the results when appropriate, including rescaling the 1σ confidence intervals (Efron & Tibshirani 1994; note that jackknife-calculated "accelerations" are insignificant). Dipole directions show negligible bias and are not corrected, but the dipole amplitudes do show bias, particularly the dipole vector and permissive fit methods (methods 3 and 4).

Table 1 shows the dipole apex and velocity of the four fitting methods for number and flux. Figure 4 shows that all values are consistent with the CMB dipole vector (direction and velocity). A comparison of each dipole vector to the CMB yields p-values $\geqslant 0.64$ for number and $\geqslant 0.35$ for flux based on a χ^2 test with three degrees of freedom. Surprisingly, the permissive fit method, which is intended to omit flux outliers and clustered sources, shows a higher flux dipole amplitude than the other

---

6 http://healpix.sf.net; Górski et al. (2005)
7 Zonca et al. (2019)
8 Newville et al. (2021)
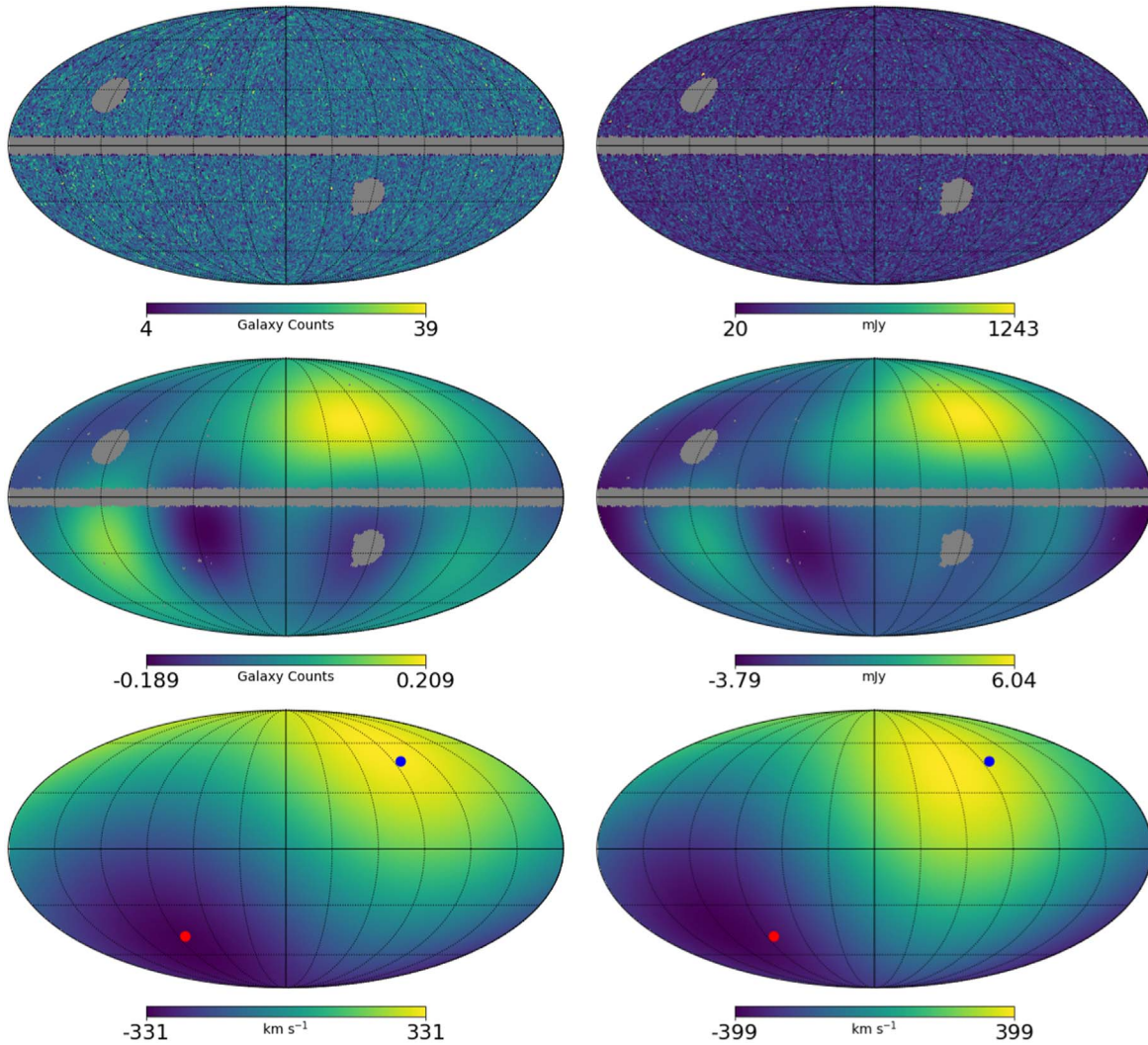
Figure 3. Top: HEALPix maps of number counts (left) and integrated flux (right) for the scaled and combined surveys in galactic coordinates. The gray regions are masked. Middle: number (left) and flux (right) mean-subtracted maps smoothed to 1 sr. These maps should not be confused with fractional difference maps, which are unitless. Bottom: spherical harmonic fit velocity maps for number (left) and flux (right). The blue and red points indicate the apex and nadir of the CMB dipole (Planck Collaboration et al. 2020a, 2020b).

methods (although it is consistent with these and the CMB). Figure 3 (bottom) shows the velocity dipole maps for number and flux for the SH fit method.

6. Discussion

Why do these results differ from previous studies that reject the CMB dipole amplitude? As usual, when astronomical observations are used to obtain subpercent measurements, systematics are a concern, and there are differences in approach and data sources to consider. Sky completeness is known to impose a strong bias on results (e.g., Gibelyou & Huterer 2012; Siewert et al. 2021), and this work is among the most complete with $f_{sky} = 0.90$. The source density is comparable to previous work (see, e.g., Siewert et al. 2021), the angular resolution is higher in the VLASS but not the RACS, and the sensitivity is better at comparable frequencies. Our results have larger uncertainties on the dipole direction than most previous work, but this is likely to be due in part to the smaller amplitude, given the only slightly larger source catalog. Also, previous work uses integrated fluxes, which are sensitive to source sizes,
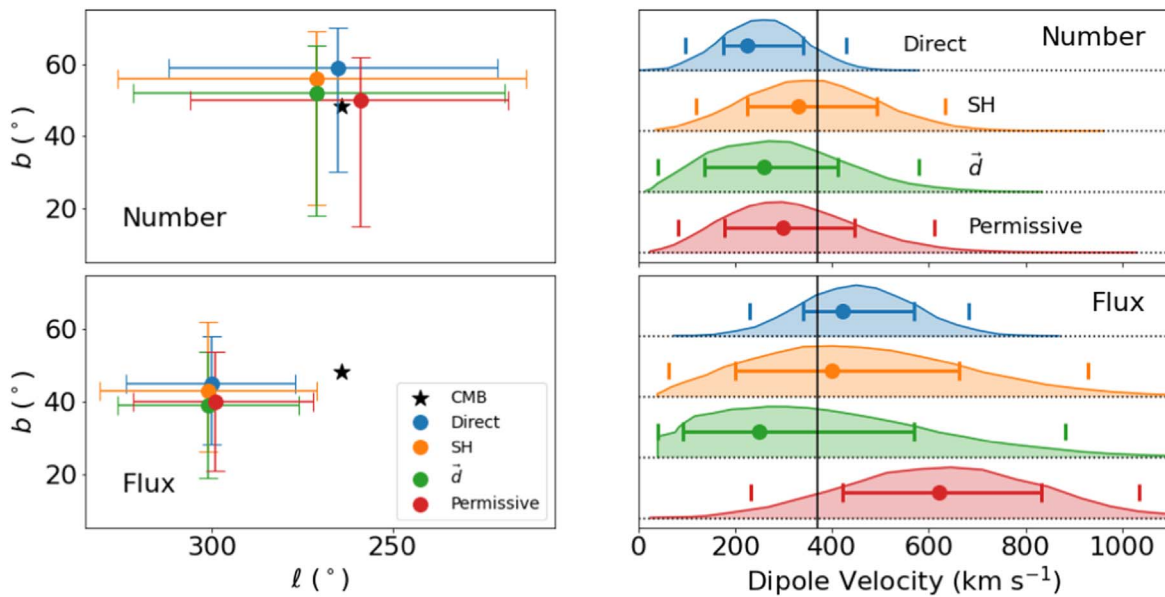
Table 1
Radio Galaxy Dipole Results

| # | Method | Quantity | Apex | | Velocity |
			$\ell(°)$	$b\ (°)$	(km s^{-1})
1	Direct	Number	265^{+47}_{-44}	59^{+11}_{-29}	225^{+116}_{-51}
		Flux	300^{+24}_{-23}	45^{+13}_{-17}	422^{+147}_{-83}
2	SH	Number	271^{+55}_{-58}	56^{+13}_{-35}	331^{+161}_{-107}
		Flux	301^{+30}_{-30}	43^{+19}_{-17}	399^{+264a}_{-199}
3	*d*	Number	271^{+51}_{-52}	52^{+13}_{-34}	259^{+152a}_{-124}
		Flux	301^{+25}_{-25}	39^{+15}_{-20}	250^{+320a}_{-160}
4	Permissive	Number	259^{+47}_{-41}	50^{+12}_{-35}	297^{+150a}_{-120}
		Flux	299^{+23}_{-27}	40^{+14}_{-19}	622^{+211a}_{-200}
	CMB	Temperature	264.0	48.3	369.8

Note.
[a] Bias-corrected velocities.

resolution, and surface brightness sensitivity in a frequency-dependent manner. This was the motivation for employing peak fluxes instead.

Figure 4. Left: dipole apex measured from radio source number counts (top) and fluxes (bottom) using the methods listed in Table 1. The star indicates the CMB dipole apex, and error bars are 1σ uncertainties. Right: dipole velocity measured from radio source number counts (top) and fluxes (bottom). The vertical line indicates the observed CMB dipole. The envelopes show the error distributions in dipole amplitudes, and the vertical tick marks show 1σ and 2σ uncertainties.

Intriguingly, Siewert et al. (2021) found that the measured dipole amplitude obtained from source counts decreases with increasing frequency, up to 1.4 GHz (NVSS). However, an extrapolation of their fit of $\mathcal{D}_N$ versus ν predicts a value at 3 GHz of more than twice what we measure. Nevertheless, it could be that the solar peculiar motion is best measured at higher radio frequencies.

While the results of this study are consistent with the CMB dipole vector, they are not necessarily inconsistent with previous work because the amplitude uncertainty distributions have large high-velocity tails (Figure 4). For example, the vector method (**d**) for number density that is most directly comparable to the Secrest et al. (2021) methods and result has a $+3\sigma$ value of 740 km s^{-1}, which is roughly consistent with the Secrest et al. (2021) amplitude measurement.

The Appendix presents an empirical examination of our analysis assumptions and possible measurement systematics. We assess the elevation-dependent source counts in the surveys, the ability of each survey alone to measure the dipole, the impact of the selected flux limit, the choice of peak versus total flux, and the fine-tuning of the spectral index used to combine the two surveys. Nearly all of these tests recover dipoles consistent with the CMB, albeit with larger uncertainties in the dipole amplitude and direction than those listed in Table 1.

7. Conclusions

Contrary to previous studies, this work shows that the observed dipole in extragalactic source counts and fluxes is consistent with an observer-induced CMB dipole; there is no discrepancy in direction or amplitude between radio sources and the CMB. This aligns with already CMB-consistent observations of local large-scale structures, the tSZ effect, and supernovae (Rowan-Robinson et al. 1990; Lavaux et al. 2010; Planck Collaboration et al. 2020c; Horstmann et al. 2021). It seems plausible that future all-sky extragalactic surveys may achieve the depth and fidelity to either confirm

that the CMB dipole is nearly all observer induced or to identify a contribution that is cosmological.

A number of refinements in the above methods can be explored, including employing a broken or two-index power law for source counts and spectral indices following Siewert et al. (2021), using survey depth- and artifact-weighted maps, or the more formal (and perhaps more rigorous) analyses employed by previous investigators. With the additional VLASS epochs and the ASKAP follow-on to RACS, the surveys themselves will also improve soon, both in depth and calibration and in processing refinement.

Appendix

Here we examine assumptions used in the data selection and analysis, particularly regarding the combination of the two

---

[9] http://www.astropy.org

radio surveys. The goal is twofold: (1) to build confidence in the dipole measurement methods in light of the disparate prior results and (2) to explore possible reasons for discrepancies.

Because the dipoles obtained from galaxy counts and flux are similar for all different fitting methods (Table 1), the following tests focus on galaxy counts and use the permissive least-squares fitting method. Unless otherwise specified, all selection parameters and methods are unchanged from Section 4. For example, when we examine the two radio continuum surveys individually, the analysis, flux limits, and other parameters are unchanged unless explicitly described.

Appendix A
Single-survey Tests

To assess the impact of combining two disparate radio surveys, we examine the source-count dipole found in each survey alone. As seen in Figure 1, the surveys are not perfectly uniform, particularly as a function of declination. Figure 5 shows the areal source density versus equatorial coordinates. The VLASS shows a 16% decrease from declination $-15°$ to $-40°$, and the RACS shows a 6% decrease for $\delta > +25°$. Neither survey shows trends in R.A. (the lowered source density in the VLASS in Figure 5 (left) is caused by the diminished source density contribution from $\delta < -15°$ regions, which affects all R.A. bins).

When we fit the VLASS or RACS alone without trimming the declination range, we obtain a dipole with an apex near the apex of each survey (the equatorial poles) because the reduced galaxy density at lower elevations (lower declinations for the VLASS, and higher declinations for the RACS) produces a

gradient. Implementing a declination-based correction factor for source counts does not completely correct the problem because there is a spatial structure in the problematic declination ranges (Figure 1).

We also examined single-survey source-count dipoles obtained by omitting the lower-density declinations indicated in Figure 5. If we trim the VLASS to the declinations that show no reduction in galaxy density, $\delta > -15°$ and $f_{sky} = 0.58$, then the dipole nadir aligns with the missing data, directed toward the south equatorial pole: the apex is 683^{+194}_{-113} km s^{-1} toward 93^{+8}_{-4}, 56^{+20}_{-16} (degrees, Galactic coordinates). However, using the RACS only we recover a galaxy count dipole that is consistent with the joint analysis, albeit with substantially larger uncertainties, which is a combination of fewer overall sources and significantly reduced sky coverage. For the RACS catalog with $\delta < +25°$ clipping, $f_{sky} = 0.66$, and we obtain a dipole with amplitude 644^{+319}_{-148} km s^{-1} toward 292^{+21}_{-23}, 13^{+18}_{-20} (degrees).

If we fix the dipole direction to that obtained using the combined surveys and fit only for the amplitude, the VLASS, trimmed to $\delta > -15°$, has a reduced and less significant amplitude of 289^{+251}_{-192} km s^{-1} compared to the joint fit. This is due in part to the low-count pixel regions seen near the dipole apex (Figure 1, left). For the RACS, trimmed to $\delta < +25°$, the amplitude is higher but has a similar uncertainty: 428^{+203}_{-212} km s^{-1}. Both of these single-survey values are consistent with the CMB dipole amplitude. Given the amplitude uncertainties, however, this result cannot address the dipole amplitude frequency-dependence suggested by Siewert et al. (2021).
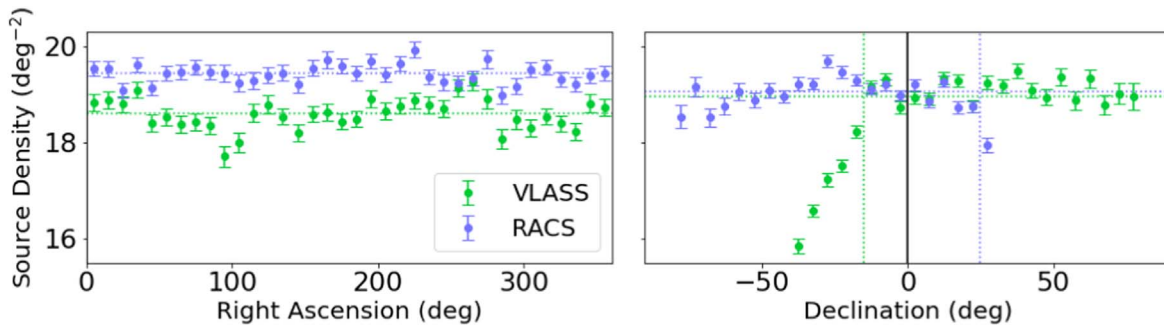
Figure 5. Mean VLASS and RACS areal density vs. R.A. (left) and declination (right) in 5° increments. The vertical dotted lines denote the declination cuts used for the single-survey dipole fitting ($\delta > -15°$ for the VLASS and $\delta < +25°$ for the RACS), and the horizontal dotted lines indicate the median values. The vertical black line shows the declination where the two surveys are cut for the joint analysis. The lower source density seen in the VLASS vs. R.A. is caused by the falloff in source counts for $\delta < -15°$. When the indicated declination cut is applied, the source density in the VLASS matches that of the RACS.

Appendix B
Flux Limits

The survey flux limits were selected to avoid the incompleteness turnover at low fluxes and the shot noise of rarer objects at high fluxes. Blake & Wall (2002) show a change in the observed radio galaxy dipole measurements with a change in lower flux limit, and we assess the impact of the lower flux limit by doubling the lower flux limit on the VLASS, propagating it to RACS, and following the procedures described in Sections 3 and 4. Doubling the lower flux limit roughly halves the source catalog to 54% of the original catalog (because the exponent on $N(>S) \propto S^{-x}$ is $x = 1$), correspondingly lowering the S/N. With the reduced catalog, we reproduce and recover the source-count dipole, but with larger uncertainties (as expected): 657^{+429}_{-135} km s^{-1} toward 309^{+24}_{-44}, 27^{+20}_{-27} (degrees).

Appendix C
Peak versus Total Flux

To explore the choice of using the peak flux density from the VLASS and RACS surveys rather than the more canonical total source flux density, we repeated the analysis using the total source flux in both catalogs. For simplicity, we retain the flux limits used for the VLASS and scale these to the RACS using the median spectral index obtained from the total flux ratio in the overlap region (Section 3). In this case, $\alpha = 0.81$, the count index x is unchanged, and we recover the dipole: 527^{+195}_{-132} km s^{-1} toward 241^{+17}_{-49}, 66^{+10}_{-19} (degrees), which is consistent with the CMB vector (a χ^2_3 test p-value of 0.25). For the reasons described in Section 3, the peak flux densities are preferable, but the total flux densities can also be used to detect a galaxy dipole that is consistent with the CMB.

Appendix D
Radio Spectral Index

The fine-tuning of the spectral index α used to combine the surveys is a concern because the spectral index shows a large range of values among the VLASS–RACS overlap sample (Section 3). In our treatment, we employ the median spectral index or the flux-weighted median spectral index of the overlap sample. When the spectral index is incorrect, a dipole is produced that points toward the equatorial hemisphere favored by the overweighted survey. Fine-tuning is required to equalize the two hemispheres to less than 1% in order to detect the dipole signal.

In order to address this fine-tuning problem and the large intrinsic dispersion in spectral indices, we use the overlap region between the surveys ($|\delta| < 10°$) to find the RACS flux limits that produce a match between the areal source densities of the two surveys given the VLASS flux limits. The upper RACS flux limit has a negligible impact on the source counts. Adjusting the lower RACS flux limit to obtain matching source-count densities in the overlap region between the two surveys produces a limit that agrees with the flux limit obtained from the median spectral index to within 1%. It is notable that the combined overlap catalog obtained from matching VLASS to RACS sources (Section 3.1) is not identical to the individual flux-limited VLASS and RACS catalogs in the overlap region. It is reassuring that the selection outcomes agree between these disparate approaches to catalog matching.

Ultimately, choosing a median spectral index and the above count-matching approach are equivalent, but the latter may be more satisfying from a fine-tuning perspective. The count-matching approach could be modified to a flux-matching approach to measure the radio flux dipole.

ORCID iDs

Jeremy Darling ⓘ https://orcid.org/0000-0003-2511-2060

References

Astropy Collaboration, Robitaille, T. P., Tollerud, E. J., et al. 2013, A&A, 558, A33

Blake, C., & Wall, J. 2002, Natur, 416, 150

Condon, J. J., Cotton, W. D., Greisen, E. W., et al. 1998, AJ, 115, 1693

Croft, R. A. C. 2021, MNRAS, 501, 2688

Darling, J., Truebenbach, A. E., & Paine, J. 2018, ApJ, 861, 113

Ding, F., & Croft, R. A. C. 2009, MNRAS, 397, 1739

Efron, B., & Tibshirani, R. J. 1994, An Introduction to the Bootstrap (Boca Raton, FL: CRC Press)

Ellis, G. F. R., & Baldwin, J. E. 1984, MNRAS, 206, 377

Gibelyou, C., & Huterer, D. 2012, MNRAS, 427, 1994

Gordon, Y. A., Boyce, M. M., O'Dea, C. P., et al. 2021, ApJS, 255, 30

Górski, K. M., Hivon, E., Banday, A. J., et al. 2005, ApJ, 622, 759

Hale, C. L., McConnell, D., Thomson, A. J. M., et al. 2021, PASA, 38, e058

Horstmann, N., Pietschke, Y., & Schwarz, D. J. 2021, arXiv:2111.03055

Hunter, J. D. 2007, CSE, 9, 90

Intema, H. T., Jagannathan, P., Mooley, K. P., & Frail, D. A. 2017, A&A, 598, A78

Lacy, M., Baum, S. A., Chandler, C. J., et al. 2020, PASP, 132, 035001

Lavaux, G., Tully, R. B., Mohayaee, R., & Colombi, S. 2010, ApJ, 709, 483

McConnell, D., Hale, C. L., Lenc, E., et al. 2020, PASA, 37, e048

Murphy, T., Mauch, T., Green, A., et al. 2007, MNRAS, 382, 382

Newville, M., Otten, R., Nelson, A., et al. 2021, lmfit/lmfit-py: v1.0.3, Zenodo, doi:10.5281/zenodo.5570790

Paine, J., Darling, J., Graziani, R., & Courtois, H. M. 2020, ApJ, 890, 146

Planck Collaboration, Aghanim, N., Akrami, Y., et al. 2020a, A&A, 641, A1

Planck Collaboration, Aghanim, N., Akrami, Y., et al. 2020b, A&A, 641, A3

Planck Collaboration, Akrami, Y., Ashdown, M., et al. 2020c, A&A, 644, A100

Price-Whelan, A. M., Sipőcz, B. M., Günther, H. M., et al. 2018, AJ, 156, 123

Rengelink, R. B., Tang, Y., de Bruyn, A. G., et al. 1997, A&AS, 124, 259

Rowan-Robinson, M., Lawrence, A., Saunders, W., et al. 1990, MNRAS, 247, 1

Rubart, M., & Schwarz, D. J. 2013, A&A, 555, A117

Secrest, N. J., von Hausegger, S., Rameez, M., et al. 2021, ApJL, 908, L51

Siewert, T. M., Schmidt-Rubart, M., & Schwarz, D. J. 2021, A&A, 653, A9

Singal, A. K. 2011, ApJL, 742, L23

Sivia, D. S., & Skilling, J. 2006, Data Analysis—A Bayesian Tutorial (2nd ed.; Oxford: Oxford Univ. Press)

Smoot, G. F., Gorenstein, M. V., & Muller, R. A. 1977, PhRvL, 39, 898

Taylor, M. B. 2005, in ASP Conf. Ser. 347, Astronomical Data Analysis Software and Systems XIV, ed. P. Shopbell, M. Britton, & R. Ebert (San Francisco, CA: ASP), 29

Tiwari, P., & Aluri, P. K. 2019, ApJ, 878, 32

van der Walt, S., Colbert, S. C., & Varoquaux, G. 2011, CSE, 13, 22

Wright, E. L., Eisenhardt, P. R. M., Mainzer, A. K., et al. 2010, AJ, 140, 1868

Zonca, A., Singer, L., Lenz, D., et al. 2019, JOSS, 4, 1298